# THE XPS STUDY OF PYROCHLORE MATRIXES FOR THE RADIOACTIVE WASTE DISPOSAL

by

***Anton Yu. TETERIN*** [1], ***Konstantin I. MASLAKOV*** [1], ***Yury A. TETERIN*** [1*], ***Kirill E. IVANOV*** [1], ***Sergei V. YUDINTSEV*** [2], ***Sergei V. STEFANOVSKY*** [3], ***Tatyana S. LIVSHITS*** [2], ***and Mariya I. LAPINA*** [2]

[1]Russian Research Centre "Kurchatov Institute", Moscow, Russia
[2]Institute of Geology of Ore Depositions of RAS, Moscow, Russia
[3]Moscow NPO "Radon", Moscow, Russia

Scientific paper
UDC: 621.039.74/.76:666.3-13:543.428.4
DOI: 10.2298/NTRP1003157T

**Two pyrochlore ceramic samples were studied in this work. The X-ray diffraction and the scanning electron microscopy showed that the ceramics with the calculated composition $CaThSn_2O_7$ was formed by the dominating pyrochlore phase with the traces of thorianite and hematite, while the $CaThZr_2O_7$ ceramics – by the dominating pyrochlore phase with the minor admixtures of thorianite and perovskite. The real compositions of pyrochlore phases determined by the scaning electron microscopy are $Ca_{0.88}Th_{0.92}Sn_2O_{6.72}$ and $Ca_{0.84}Th_{0.80}Zr_2O_{6.44}$. On the basis of the X-ray photoelectron spectral parameters of the outer and core electrons in the binding energy range of 0-1250 eV it was found that tin, zirconium and thorium in pyrochlore are at least 93%-94% tetravalent. Sn-O and Zr-O interatomic distances in $BO_6$-octahedrons in the pyrochlore were found to be 0.210 nm and 0.220 nm, respectively, and these octahedrons are possible to be tetragonaly distorted.**

*Key words: X-ray photoelectron spectroscopy, outer and inner valence molecular orbitals, pyrochlore, radioactive waste disposal*

## INTRODUCTION

Processing of the irradiated spent fuel from the nuclear power plants produces a lot of radioactive wastes including the high-level ones (HLW). The most dangerous HLW radionuclides are actinides and some long-lived decay products ($^{95}Zr$, $^{99}Tc$, $^{125}Sn$, *etc*.). They are supposed to be included into the firm, durable, protective matrixes for the subsequent underground disposal. The correct choice of materials is the key safety problem during the HLW processing. Understanding of the chemical processes in the matrixes requires knowledge of the physical and chemical states of radionuclides and matrix elements.

X-ray photoelectron spectroscopy (XPS) proved to be the most adequate tool for tackling this problem. In particular, structural changes in pyrochlore during the amorphization by accelerated ions were studied by XPS. This work carried out the qualitative elemental and ionic analysis and studied the oxidation states of included elements for $CaThZr_2O_7$ and $CaThSn_2O_7$ ceramic samples with pyrochlore structure proposed as matrixes for the long-term storage of the HLW long-lived radionuclides.

## EXPERIMENTAL

Samples of the calculated compositions $CaThSn_2O_7$ (sample 1) and $CaThZr_2O_7$ (sample 2) were prepared from the mixtures of $CaCO_3$, $ThO_2$, $SnO_2$, and $ZrO_2$ powders, ground in an agate mortar to the size of 20 μm to 30 μm. The mixtures were pressed under 200 MPa to 400 MPa into 12 mm to 30 mm diameter and 4 mm to 5 mm high cylindrical pellets and sintered in alundum crucibles at 1500 °C to 1550 °C for 6 to 10 hours. The samples were studied by X-ray diffraction analysis (XRD) on the DRON-4 (Cu $K_\alpha$) diffractometer, as well as on the scanning (SEM/EDS: JSM-5300 with the energy-dispersion spectrometer Link ISIS) and transmission (JEM-100) electron microscopes [3-5].

XPS spectra of the studied samples were acquired with an HP5950A electrostatic spectrometer using

* Corresponding author; e-mail: teterin@ignp.kiae.ru

monochromatized $AlK_{\alpha 1,2}$ ($h\nu$ = 1486.6 eV) radiation and with an MK II VG scientific electrostatic spectrometer under 1.3 $10^{-7}$ Pa at the room temperature. The device resolution measured as the full width on the half-maximum (FWHM) of the $Au4f_{7/2}$ peak on the standard rectangular gold plate was 0.8 eV (HP 5950A) and 1.2 eV (MK II VG Scientific). The binding energies $E_b$(eV) were measured relative to the binding energy of the C1s electrons from hydrocarbons absorbed on the sample surface accepted to be equal to 285.0 eV. For the gold standard the calibration binding energies $E_b$(C1s) = 285.0 eV and $E_b(Au4f_{7/2})$ = 83.7 eV were used. The C1s XPS peak from hydrocarbon on the gold plate was observed 1.3 eV wide. The error in the determination of the binding energy and the peak widths did not exceed 0.1 eV, that of the relative peak intensity – 10%. Table 1 gives FWHMs ($\Gamma$) relative to that of the C1s peak $\Gamma$(C1s) = 1.3 eV for comparison with other studies' results [6, 7]. Sample 1 was studied as a pellet and the other samples for the XPS study were prepared from the finely dispersed powder ground in the agate mortar as a dense thick layer with a flat surface pressed in indium foil on a titanium substrate.

For all the samples the quantitative elemental and ionic analysis was done by the following ratio: $n_i/n_j = (S_i/S_j)(k_j/k_i)$, where $n_i/n_j$ is the relative concentration of the studied atoms, $S_i/S_j$ – the relative core-shell spectral intensity, and $k_j/k_i$ – the relative experimental sensitivity coefficient. The present work used the following sensitivity coefficients relative to the C1s: 1.00 (C1s), 2.64 (O1s), 4.2 ($Ca2p_{3/2}$), 6.32 (Ca2p), 8.4 (Zr3d), 4.16 ($Zr3p_{3/2}$), 17.2 ($Sn3d_{5/2}$), 31.2 ($Th4f_{7/2}$), and 3.6 ($Th5d_{5/2}$) [8]. XPS parameters of metallic Ca, CaO, $CaCO_3$, $ThO_2$, $SnO_4$, $ZrO_4$ and $CaZrO_3$, were used for the interpretation of spectra (tab. 1).

## RESULTS AND DISCUSSION

According to the SEM/EDS data, the real pyrochlore phase compositions in the studied ceramic samples are $Ca_{0.88}Th_{0.92}Sn_2O_{6.72}$ for sample 1 (assuming that all included tin is tetravalent) and $Ca_{0.84}Th_{0.80}Zr_2O_{6.44}$ for sample 2. The real surface compositions determined by XPS, except for calcium, do not differ from the SEM/EDS data within the measurement error. Calcium content was observed lower for sample 1 and higher for sample 2. It can be explained by calcium contents being different on the surface compared with that in the bulk. According to the XRD and SEM data, pyrochlore phase dominates in sample 1 with the traces of thorianite and hematite, while sample 2 besides pyrochlore phase contains the noticeable admixtures of thorianite ($ThO_2$) and perovskite phase ($CaZrO_3$) (figs. 1 and 2). The presence of hematite in sample 1 can be explained by the admixture of iron during the grinding in the metallic

**Table 1. Binding energies $E_b$ and line widths $\Gamma$[(a)] of outer MOs and core electrons of pyrochlore ceramics**

| Compound | MO [eV] | Th4f [eV] | Th5d [eV] | Zr3d, Sn3d [eV] | Zr3p [eV] | Ca2p [eV] | O1s [eV] | C1s [eV] |
|---|---|---|---|---|---|---|---|---|
| $CaThSn_2O_7$[(b) (c)] (sample 1) | 5.1 16.3<br>21.2 25.8 | 334.6 (1.1)<br>343.9 (1.1) | 86.4 (1.2)<br>93.3 (1.7) | 486.9 (1.3)<br>495.3 (1.2) | | 346.9<br>350.6 | 530.0 (1.6)<br>531.9 | 285.0 (1.3)<br>288.2 |
| $CaThZr_2O_7$[(b) (c)] (sample 2) | 6.1 16.6<br>21.5 24.6<br>30.2 34.3<br>43.2 | 333.4 (1.1)<br>343.9 | 86.4<br>93.3 | 181.6 (1.1)<br>183.9 | 331.3<br>341.3 | 346.2<br>350.1 (2.0) | 529.7 (1.6)<br>531.7<br>532.9 | 285.0 (1.3)<br>289.3 |
| $ThO_2$ | 5.8 16.5<br>22.0 25.5 | 334.3<br>343.6 | 86.3<br>93.3 | | | | 530.2 | 285.0 |
| $CaZrO_3$[(d)] | 5.3 20.6<br>20.6 24.8<br>30.0 43.6 | | | 181.7<br>183.9 | 332.3 | 350.3 | 529.8<br>531.6 | 285.0<br>289.5 |
| $ZrO_2$ | 5.6 21.3<br>30.6 | | | 182.5 | 332.8<br>346.4 | | 530.1 | 285.0 |
| $SnO_2$ | | | | 486.7<br>495.1 | | | 530.6 | 285.0 |
| Ca (metal) | –0.6 (1.2)<br>23.4<br>42.5 (1.8) | | | | | 344.7 (1.7)<br>348.4 (1.7) | | 285.0 (1.3) |
| CaO | 4.3 (2.1)<br>20.1 (2,6)<br>24.3 (2.0)<br>42.9 (1.9) | | | | | 346.0 (1.7)<br>349.7 (1.7) | 528.9 (1.4) | 285.0 (1.3) |
| $CaCO_3$ | 5.3 (2.2)<br>25.2 (2.0)<br>44.1 (1.8) | | | | | 347.3 (1.7)<br>351.0 (1.7) | 531.6 (1.6) | 285.0 (1.3)<br>289.7 (1.3) |

[(a)] FWHMS relative to that of the C1s one accepted to be equal to 1.3 eV are given in parentheses
[(b)] SEM/EDS data for bulk composition: $Ca_{0.92}Th_{0.92}Sn_2O_{6.96}$ (1) and $Ca_{0.91}Th_{0.84}Zr_{2.25}O_{7.09}$ (2) [3]
[(c)] XPS data for the surface composition: $Ca_{0.48}Th_{0.94}Sn_2O_{6.46}$ (1) and $Ca_{2.50}Th_{1.04}Zr_{2.00}O_{12.84}(Si_{1.24})$ (2), $E_b$(Si2p) = 102.8 eV
[(d)] C1s and O1s binding energies for $CO_3^{2-}$ group on the surface are marked

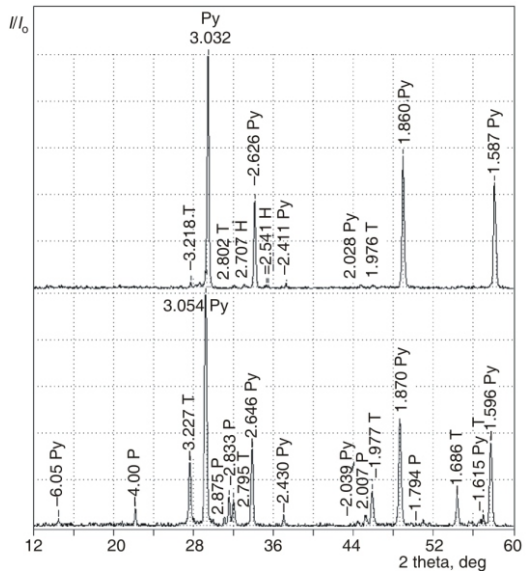


**Figure 1. XRD pictures of sample 1 (a) and 2 (b)**
*H – hematite, P – perovskite phase ($CaZrO_3$), Py – pyrochlore phase, T – thorianite*

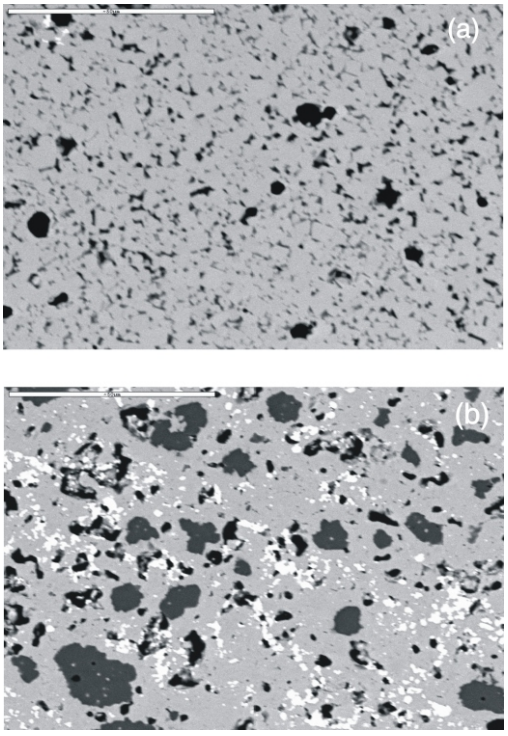


**Figure 2. Backscattered electrons images of ceramic samples 1 (a), and 2 (b); the grey spots in the picture (b) is pyrochlor, dark-grey grains – perovskite, white impurities – thorianite, and black spots – pores; the size of marks – 50 μm**

mortar. SEM image of sample 2 (fig. 2) shows pyrochlore as a basic light-grey background with small white grains of thorianite and larger dark-grey grains of perovskite-type phase distributed.

The XPS from the studied samples in the binding energy range of 0-1250 eV exhibits the peaks attributed to the included elements (fig. 3). This energy range can be subdivided into the three parts [6, 7]. The first one (0-15 eV) contains the structure related to the outer valence molecular orbitals (OVMO) formed from the incompletely filled outer electronic shells. For example, the An5f intensity (An – actinides) in the low binding energy range can be used for the evaluation of the actinide oxidation states [6, 7]. The second sub-range (15-50 eV) shows the structure due to the inner valence molecular orbitals (IVMO) formed from the completely filled low energy electronic shells. The OVMO parameters correlate with the close environment structure and, in particular, for actinide compounds, can be used for the evaluation of the An-neighbor interatomic distances [6, 7]. The third sub-range: above ~50 eV, exhibits peaks from the core electronic shells that do not significantly participate in the molecular orbitals (MO) formation. However, this sub-range can show the structure related to the spin-orbit interaction ( $E_{sl}$, eV), multiplet splitting ( $E_{ms}$, eV), many-body perturbation, dynamic effect, *etc*. Since parameters of this structure correlate with the physical and chemical properties of compounds, they can be used in the XPS studies in combination with the traditional parameters like electron binding energies, chemical shifts, and peak intensities [7]. To simplify the discussion, both the atomic and molecular terms were used in this work.

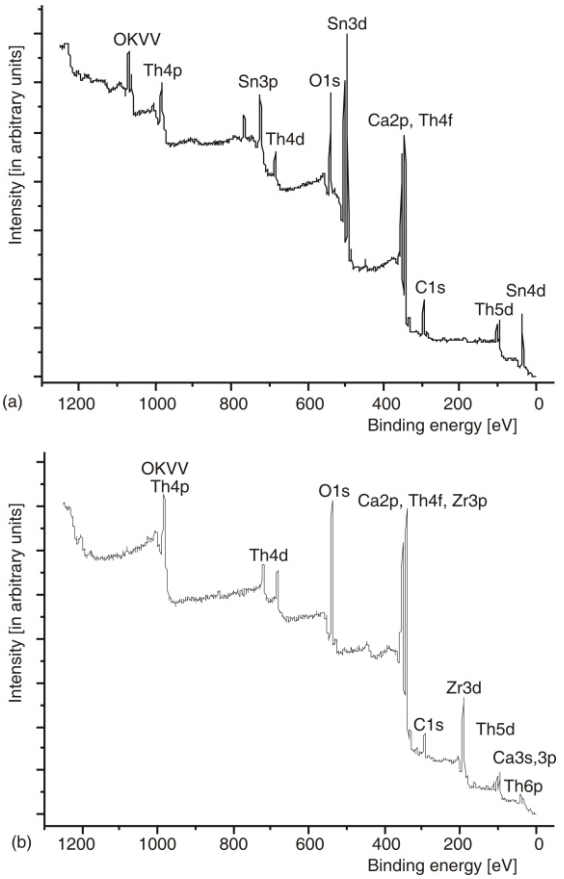


**Figure 3. Survey XPS in the binding energy range of 0-1250 eV from: (a) – sample 1, (b) – sample 2**

***Low binding energy (0-50 eV) XPS range***. This spectral range for studied samples shows two-humped OVMO structure related to the outer valence Ca4s, Th6d,7s, Sn5s,5p, Zr4d,5s, and O2p electrons, as well as the IVMO structure due to the Ca3s,3p, $Th6p_{3/2}$, Sn4d, Zr4p, and O2s electrons (fig. 4, tab. 1). Because of the high intense Sn4d peak, the background on the higher binding energy side and the low calcium concentration, the Ca3p and Ca3s peaks at 24 and 43 eV, respectively, are not observed in the spectrum from sample 1. But these peaks are well observed in the XPS from sample 2, which does not contain tin (fig. 4). These spectra allow only qualitative elemental analysis, since they appear not as separate atomic peaks but as MO-related bands. The $Th6p_{3/2}$ and O2s peaks are well observed. Low intense peaks at 9 eV and 13 eV, apparently, may be attributed to the small amount of the $CO_3^{2-}$ impurities on the sample surface. Their signature also presents in the C1s spectra (fig. 5).

***Core electron (0-1250 eV) XPS structure***. Commonly, the most intense XPS peaks are used for elemental and ionic quantitative analysis [9]. For our samples they are Ca2p, Th4f,5d, Sn3d, Zr3p,3d, and O1s (tab. 1). In case of peaks overlapping like Th4f – Zr3p for sample 2 (fig. 6), the lower intense but more separate peaks like the Th5d and Zr3d can be used. The Th4f and Ca2p peaks also somewhat overlap (fig. 6, tab. 1). The Ca2p, Th4f, and Zr3p peaks appears as typical spin-orbit split doublets with $\Delta E_{sl}$ equal to 3.7 eV and 3.9 eV for the Ca2p, 9.3 eV and 9.5 eV for the Th4f in samples 1 and 2, respectively. $E_{sl}$ for the Zr3p doublet has to be 13.6 eV [10]. The considered XPS peaks were observed relatively sharp and single. It confirms the X-ray diffraction data on the high monophaseness of the studied samples.

The $Th4f_{7/2}$ spectrum from sample 1 exhibits a 6% shoulder on the lower binding energy side that can be attributed to the impurity (fig. 6). The same shoulder appears in the $Th5d_{5/2}$ spectrum from sample 1 and does not appear in the spectra from sample 2. These shoulders in the $Th5d_{3/2}$ and $Th4f_{7/2}$ XPS can not be attributed to the sample charging, since a similar shoulder was not observed in the C1s XPS.

The C1s XPS peaks from samples 1 and 2 are observed symmetric with a low-intense $CO_3^{2-}$ related shoulder at 289 eV (fig. 5, tab. 1). A slight widening of the C1s peak from the sample 2 comparing to that from the sample 1 can be explained either by non-uniform charging of the sample surface or by the presence of extra hydrocarbons on the surface.

The Sn3d and Zr3d spectra from the samples 1 and 2 appear as doublets with shoulders on the lower binding energy sides. While in the Sn3d spectrum this

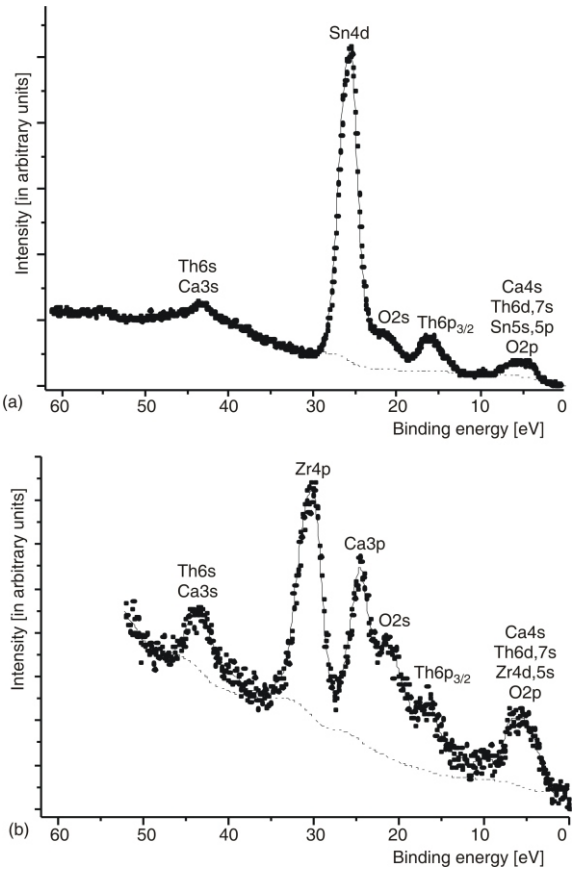


**Figure 4. Low binding energy XPS from: (a) – sample 1, (b) – sample 2**

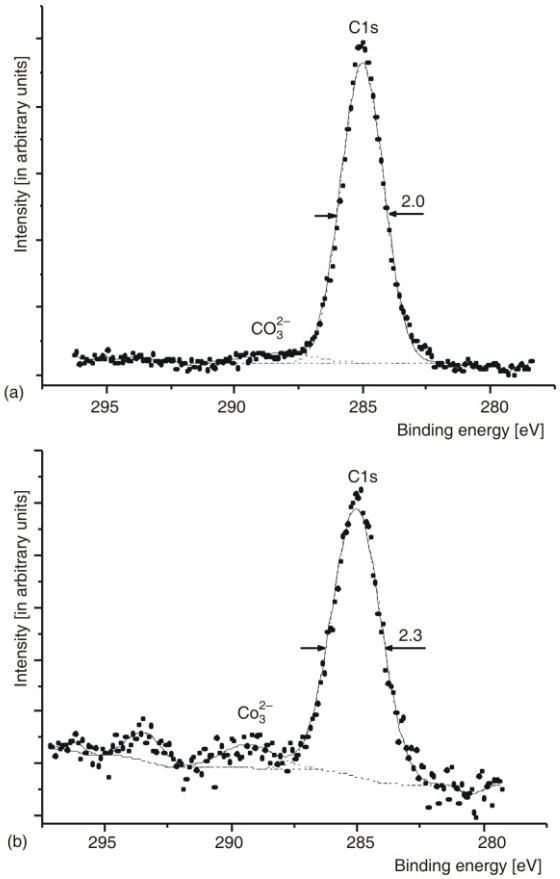


**Figure 5. C1s XPS from: (a) – sample 1, (b) – sample 2**

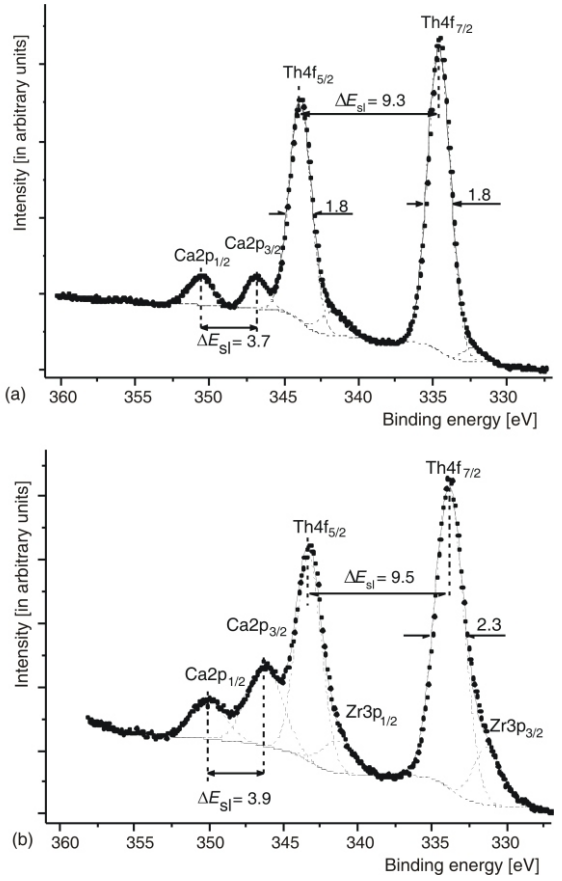


**Figure 6. Th4f and Ca2p XPS from sample 1 (a) and Th4f, Ca2p, and Zr3p XPS from sample 2 (b)**

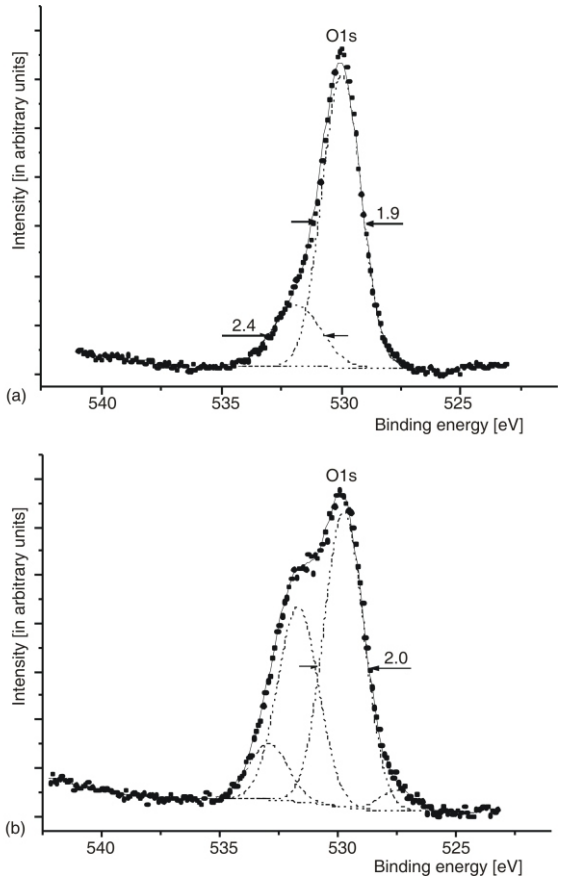


**Figure 7. O1s XPS from: (a) – sample 1, (b) – sample 2**

shoulder is negligible, the one in Zr3d spectrum reaches 7% of the basic peak intensity.

The O1s XPS from sample 1 consists of two peaks at 530.0 eV and 531.9 eV, while that from sample 2 consists of three peaks at 529.7 eV, 531.7 eV, and 532.9 eV (fig. 7). Taking into account equations [11]

$$E_b(\text{eV}) = 2.27\ R_{\text{M-O}}^{-1}[\text{nm}] + 519.4 \quad \text{(I)}$$

and

$$R_{\text{M-O}}[\text{nm}] = 2.27\ (E_b - 519.4)^{-1} \quad \text{(II)}$$

where from (II), on the basis of the O1s binding energy, one can evaluate the metal-oxygen interatomic distance $R_{\text{M-O}}$ for samples 1 and 2. Thus, for sample 1 these distances are 0.210 nm and 0.180 nm, respectively, while for the sample 2 – 0.220 nm, 0.180 nm, and 0.160 nm, respectively.

In the pyrochlore structure $A^{3+}{}_2B^{4+}{}_2O_7$ (or $A_1{}^{2+}A_2{}^{4+}B^{4+}{}_2O_7$) the $A^{3+}$ cations ($A^{2+}$ and $A^{4+}$) take the octo-co-ordinated positions relative to oxygen, and two oxygen anions $O^{2-}$ are closer to the cation $A^{3+}$ than the other six. The XRD [12] gives the Gd-O distances for $Gd_2Zr_2O_7$ – 0.228 nm and 0.250 (0.240) nm for *s*(*d*)-pyrochlore (the mean distance for *s*- and *d*--pyrochlore is 0.2445 nm and 0.2342 nm, respectively). The $B^{4+}$ anions are located in the octahedral oxygen surrounding and for $Gd_2Zr_2O_7$ the Zr–O distance is 0.209 nm for *s*-pyrochlore and 0.217 nm for *d*-pyrochlore. The EXAFS analysis [13] gives almost the same Gd-O and Zr-O distances: 0.246 nm and 0.216 nm, respectively (for *s*-pyrochlore). The EXAFS studies of $La_2Zr_2O_7$ and $La_{1-x}Ce_xZr_2O_7$ (0 $x$ 0.25) phases showed that the Zr-O distance in $La_2Zr_2O_7$ is about 0.210 nm and it grows insignificantly (to 0.212 nm) as $x$ increases to 0.25 [14].

The obtained results show that the Zr-O distance in pyrochlore (*s*-pyrochlore with strong superstructural reflections, *i. e.* with maximum cation order) is about 0.210 nm to 0.220 nm. It agrees with the distances calculated in this work by formula (II). Therefore, the distances Sn-O in sample 1 and Zr-O in sample 2 can be accepted as 0.210 nm and 0.220 nm, respectively. The lower Sn-O distance compared to Zr-O, correlates well with different ion radii in the octahedral oxygen surrounding: 0.069 nm for $Sn^{4+}$ and 0.072 nm for $Zr^{4+}$ [15].

Since the O1s binding energy can be measured with the accuracy to within 0.1 eV, the interatomic distances can be also evaluated accurately. As it follows from eq. (I), the O1s binding energy decreases as the interatomic distance $R_{\text{M–O}}$ grows. Therefore, one can conclude that the value of 0.160 nm is too low to be observed in ceramics, and it can be attributed rather to water absorbed on the sample surface.

The low binding energy component of the O1s XPS from sample 1 associated to Sn-O binding is about 5

times more intense than the higher binding energy one, fig. (7a). The lower intense component corresponding to the distance of 0.180 nm can be attributed to the surface or impurity oxygen. The other way of interpretation can be a distortion of the $SnO_6$ octahedron along the c-axis, for example, the tetragonal compression due to the unequal distribution of the $Ca^{2+}$ and $Th^{4+}$ cations which results in approaching of one or two oxygen anions $O^{2-}$ to the central $Sn^{4+}$ ion up to 0.180 nm.

In sample 2 the low binding energy component of the O1s XPS can be associated with the error during the O1s peak decomposition, fig. (7b). The second and the third component of the O1s XPS from sample 2 are associated with the oxygen ions from the first co-ordinated sphere of Zr in $ZrO_6$ octahedrons in pyrochlore ($R_{Zr\text{-}O}$ = = 0.220 nm) and perovskite ($R_{Zr\text{-}O}$ = 0.180 nm) structures. The third low intense component apparently must be associated with surface water. It has to be noted that *e. g.*, in the $ZrO_2$ structure around Zr ion with septenary co-ordination relative to oxygen, three oxygens are at 0.207 nm, and the other four – at 0.221 nm. The next closest oxygen not belonging to the first Zr co-ordinating sphere is at 0.358 nm [16]. For this surrounding the XPS must consist of the two peaks at 530.4 eV and 529.7 eV with the intensity ratio of 4/3.

***Quantitative analysis results***. The increase in error in the quantitative elemental and ionic analysis of the samples can be explained by the extra XPS structure due to the multiplet splitting and secondary electronic processes (many-body perturbation and dynamic effect). The surfaces (~5 nm) of the studied samples were found to have the following composition relative to two atoms of tin (sample 1) and two atoms of zirconium (sample 2)

$$Ca_{0.48}Th_{0.94}Sn_2O^{I}_{5.48}(O)O^{II}_{0.98}(OH^{-})C^{I}_{4.46}(CH_3) \; C^{III}_{0.12}(CO_3^{2}) \qquad (1)$$

$$Ca_{0.78}(CaO)Th_{1.04}Zr_2O^{I}_{6.86}(O)Ca_{1.72} [Ca(OH)_2]Si_{1.24}O^{II}_{5.92}(OH^{-},SiO_2)O^{III}_{0.06}(H_2O)C^{I}_{3.36} (CH_3)C^{III}_{0.16}(CO_3^{2}) \qquad (2)$$

where $O^{I}(O)$, $O^{II}(OH^{1-}, SiO_2)$, and $O^{III}(H_2O)$ – oxygen atoms from oxide, hydroxyl group, and water. The surfaces of the studied samples may contain impurities of $CO_3^{2-}$ groups, which can participate in the formation of calcium carbonate. The obtained data slightly differ from the SEM/EDS analysis results for the bulk samples

$Ca_{0.48}Th_{0.94}Sn_2O_{6.46}$ (1) and
$Ca_{0.78}Th_{1.04}Zr_{2.00}O_{6.86}$ (2) – XPS data for the surface,

$Ca_{0.92}Th_{0.92}Sn_2O_{6.96}$ (1) and
$Ca_{0.91}Th_{0.84}Zr_{2.25}O_{7.09}$ (2) – SEM/EDS data for the bulk.

This difference can be explained by the fact that the XPS analysis reflects the surface (5-10 nm) composition. The XPS shows that calcium on the surface of the sample 1 apparently presents as $Ca(OH)_2$ and its surface concentration is twice lower than the bulk one.

## CONCLUSIONS

- Ceramic sample of the calculated composition $CaThSn_2O_7$ is formed by the dominating pyrochlore phase with the traces of thorianite and hematite, while the $CaThZr_2O_7$ ceramics – by the dominating pyrochlore phase with the minor admixtures of thorianite and perovskite. The real pyrochlore phase compositions determined by SEM/EDS are $Ca_{0.88}Th_{0.92}Sn_2O_{6.72}$ and $Ca_{0.84}Th_{0.80}Zr_2O_{6.44}$.
- XPS study of $CaThSn_2O_7$ and $CaThZr_2O_7$ ceramics with pyrochlore structure used as matrixes for the disposal of long lived high level radioactive wastes was done. The XPS proved to be an effective method for the elemental and ionic quantitative analysis of ceramics used as matrixes for the disposal of long lived high level radioactive wastes.
- On the basis of XPS parameters of the core and outer electrons in the binding energy range of 0-1250 eV the oxidation states of the included metals were determined, quantitative elemental and ionic analysis was carried out and a conclusion on the monophaseness of the studied samples was drawn. The obtained data agree with the X-ray diffraction and SEM/EDS data.
- On the basis of the XPS parameters it was found that tin, zirconium, and thorium in pyrochlore are at least 93%-94% tetravalent. The interatomic distances Sn-O and Zr-O in $BO_6$-octahedrons in pyrochlore are 0.210 nm and 0.220 nm, respectively, and it is possible that these octahedrons are tetragonaly distorted.

## ACKNOWLEDGEMENT

This work was supported by the RFBR grants 08–03–00314 and 09-08-12000.

## REFERENCES

[1] Chen, J., Lian, J., Wang, L. M., Ewing, R. C., X-Ray Photoelectron Spectroscopy Study of Irradiation-Induced Amorphization of $Gd_2Ti_2O_7$, *Appl. Phys. Lett., 79* (2001), 13, pp. 1989-1991
[2] Chen, J., Lian, J., Wang, L. M., Ewing, R. C., Matt Farmer, J., Boatner, L. A., X-Ray Photoelectron Spectrum Interpretation, *Mat. Res. Soc. Proc., 713* (2002), pp. 501-506
[3] Laverov, N. P., Yudintsev, S. V., Stefanovsky, S. V., Jang, Y. N., On the New Actinide Matrixes with Pyrochlore Structure (in Russian), *DAN of Russia, 381* (2001), 3, pp. 399-402
[4] Laverov, N. P., Yudintsev, S. V., Stefanovsky, S. V., Jang, Y. N., Ewing, R. C., Synthesis and Examination

of New Actinide Pyrochlores, *Mat. Res. Soc. Symp. Proc., 713* (2002), pp. 337-344
[5] Yudintsev, S.V., Structural-Chemical Approach to the Choice of Crystalline Matrixes for Immobilization of Actinides, *Geol. of Ore Depos., 45* (2003), 2, pp. 172-187
[6] Utkin, I. O., Teterin, Yu. A., Terekhov, V. A., Ryzhkov, M. V., Teterin, A. Yu., Vukchevich, L., X-Ray Spectral Studies of the Electronic Structure of Uranyl Fluorite $UO_2F_2$, *Nuclear Technology & Radiation Protection, 2* (2004), 19, pp. 15-23
[7] Teterin, Yu. A., Ryzhkov, M. V., Teterin, A. Yu., Panov, A. D., Nikitin, A. S., Ivanov, K. E., Utkin, I. O., The Peculiarities of Chemical Bond Nature of Trioxide $\gamma$-$UO_3$.*Nuclear Technology & Radiation Protection, 1-2* (2002), 17, pp. 3-12
[8] ***, Practical Surface Analysis by Auger and X-Ray Photoelectron Spectroscopy (Eds. M. P. Seah, D. Briggs), John Wiley & Sons, Chichester, UK, 1983
[9] Nefedov, V. I., X-Ray Photoelectron Spectroscopy of Chemical Compounds (in Russian), Himiya, Moscow 1984, p. 256
[10] Fuggle, J. C., Martensson, N., Core-Level Binding Energies in Metals, *J. Electr. Spectr. Relat. Phenom, 21* (1980), pp. 275-281
[11] Sosulnikov, M. I., Teterin, Yu. A., XPS Study of Calcium, Strontium, Barium and Their Oxides, *DAN of USSR, 317* (1991), 2, pp. 418-421
[12] Moriga, T., Yoshiasa, A., Kamaru, F., Koto, K., Yoshimura, M., Somiya, S., Crystal Structure Analyses of the Pyrochloree and Fluorite-Type $Zr_2Gd_2O_7$ and Anti-Phase Domain Structure, *Solid State Ionics, 31* (1989), 4, pp. 319-328
[13] Uehara, T., Koto, K., Emura, S., Kanamaru, F., EXAFS Study of the Fluorite and Pyrochloree Compounds in the System $ZrO_2$-$Gd_2O_3$, *Solid State Ionics, 23* (1987), pp. 331-337
[14] Yokoi, H., Matsui, T., Ohno, H., Kobayashi, K., EXAFS Study of $(La_{1-x}Ce_x)Zr_2O_7$, *Mat. Res. Soc. Symp. Proc., 353* (1995), pp. 783-789
[15] Shannon, R. D., Revised Effective Ionic Radii and Systematic Studies of Interatomic Distances in Halides and Chalcogenides, *Acta Cryst. A., 32* (1976), 5, pp. 751-767
[16] Wells, A., Structural Inorganic Chemistry, Moscow, Mir, 2, 1987, p. 695

Received on February 25, 2010
Accepted on October 19, 2010

---

**Антон Ј. ТЕТЕРИН, Константин И. МАСЛАКОВ, Јурај А. ТЕТЕРИН, Кирил Е. ИВАНОВ, Сергеј В. ЈУДИНЦЕВ, Сергеј В. СТЕФАНОВСКИ, Татјана С. ЛИФШИЦ, Марија И. ЛАПИНА**

## ПРОУЧАВАЊЕ РЕНДГЕН-ИНДУКОВАНОМ ФОТОЕЛЕКТРОНСКОМ СПЕКТРОСКОПИЈОМ ПИРОХЛОРНИХ МАТРИКСА ЗА ОДЛАГАЊЕ РАДИОАКТИВНОГ ОТПАДА

У овом раду проучавани су узорци пирохлорне керамике. Методе рендген-индуковане фотоелектронске спектроскопије и скенирајуће електронске микроскопије показале су да је керамички материјал прорачуном одређеног састава $CaThSn_2O_7$ формиран са доминантном пирохлорном фазом и траговима торијанита и хематита, док у саставу $CaThZr_2O_7$ керамике поред доминантне пирохлорне фазе има и мањих додатака торијанита и перовскита. Реални састави пирохлорних фаза одређених овим методама су $Ca_{0.88}Th_{0.92}Sn_2O_{6.72}$ и $Ca_{0.84}Th_{0.80}Zr_2O_{6.44}$. На основу рендген-индукованих спектралних параметара електрона у електронском омотачу и језгру, у опсегу енергије веза од 0 eV–1250 eV, утврђено је да су калај, цирконијум и торијум у пирохлору најмање 93%–94% тетравалентни. Одређене Sn–O и Zr–O међуатомске удаљености у $BO_6$-октаедрима у пирохлору су 0.210 nm и 0.220 nm, респективно, и могуће је да су ови октаедри тетрагонално деформисани.

*Кључне речи: рендген-индукована фотоелектронска спектроскопија, спољашње и унутрашње валентне молекулске орбитале, пирохлор, одлагање радиоактивног отпада*